ACS APPLIED NANO MATERIALS
Cite This: ACS Appl. Nano Mater. 2019, 2, 1920−1929
Article
www.acsanm.org

Environmentally Friendly Zr-Based Conversion Nanocoatings for Corrosion Inhibition of Metal Surfaces Evaluated by Multimodal X-ray Analysis

Xiaoyang Liu,[†] Donald Vonk,[‡] Hua Jiang,[†] Kim Kisslinger,[⊥] Xiao Tong,[⊥] Mingyuan Ge,[§] Evgeny Nazaretski,[§] Bruce Ravel,[∥] Kate Foster,[‡] Stanislas Petrash,[#] and Yu-chen Karen Chen-Wiegart*[,†,§]

[†]Department of Materials Science and Chemical Engineering, Stony Brook University, Stony Brook, New York 11794, United States
[‡]Henkel Corporation, Madison Heights, Michigan 48071, United States
[§]National Synchrotron Light Source II, Brookhaven National Laboratory, Upton, New York 11973, United States
[∥]National Institute of Standards and Technology, Gaithersburg, Maryland 20899, United States
[⊥]Center for Functional Nanomaterials, Brookhaven National Laboratory, Upton, New York 11973, United States
[#]Henkel Corporation, Bridgewater, New Jersey 08807, United States

Supporting Information

ABSTRACT: Chemical conversion coating as an effective corrosion inhibition has wide range of applications in industries and is of great expectation to be environmentally friendly and cost-effective. Zirconium-based (Zr-based) conversion coating using hexafluorozirconic acid with copper (Cu) additive on low carbon steel which improves anticorrosion and adhesion properties was studied using synchrotron X-ray and electron-based techniques. To understand the elemental evolution during coating formation process, *in situ* synchrotron X-ray fluorescence (XRF) microscopy has been applied to observe Zr, Cu, iron (Fe), and zinc (Zn) concentration evolution. By quantifying the density, average size, and size distribution of the cluster as a function of time and temperature, the growth mechanism of the coating can be concluded as a reaction-controlled mechanism. X-ray absorption near edge structure and X-ray photoelectron spectroscopy (XPS) were used to characterize the composition of the Cu-rich clusters embedded in the coating which was determined to be mainly Cu_2O, Cu, and CuF_2; the cluster composition varies from the surface to the internal region as determined by the depth-profiling of XPS. Our study shed light on the chemical and morphological evolution in environmentally friendly surface conversation coating and demonstrated new methodology in studying the coating formation via *in situ* synchrotron XRF.

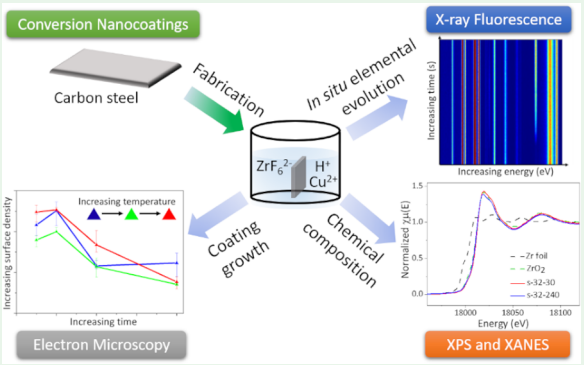

KEYWORDS: *zirconium conversion film, XANES, deposition mechanism, XRF mapping, corrosion protection*

1. INTRODUCTION

Metal corrosion is a serious problem that costs US industry approximately $250 billion annually.[1] Corrosion can be controlled by various methods such as cathodic/anodic protection, corrosion inhibitors, and anticorrosion organic coatings.[2−4] Among the methods, surface chemical conversion coating methods have been applied in the automobile, appliance, and aerospace industries and are of great importance. In the surface chemical conversion process, the surface of metal substrates is first subjected to a chemical pretreatment to create a surface coating. Such coating can significantly improve anticorrosion properties of the metals and enhance the adhesion of the paint layers subsequently applied on top of the coating.[5] In conventional conversion coating process, chromate and phosphate containing conversion coatings have been widely used in automotive, agriculture, and appliance industries. However, there is a strong motivation to remove these hazardous components from the surface treatment process. First, the chromate compounds are toxic and carcinogenic. Therefore, U.S. Department of Defense has prohibited the usage and delivery of items containing more than 0.1 wt % hexavalent chromium.[6] In addition, for tricationic phosphating conversion coating, because phosphate discharges from the concentrated phosphate baths, it has

Received: December 20, 2018
Accepted: March 14, 2019
Published: March 14, 2019

DOI: 10.1021/acsanm.8b02309
ACS Appl. Nano Mater. 2019, 2, 1920−1929

Table 1. Conversion Coating Treatment Conditions Used for the Low Carbon Steel (LCS) Substrates To Study the Evolution of the Coating Morphology

	time (s)				
temperature (°C)	30	60	120	240	600
22	sample (s)-22-30	s-22-60	s-22-120	s-22-240	s-22-600
32	s-32-30	s-32-60	s-32-120	s-32-240	
42	s-42-30	s-42-60	s-42-120	s-42-240	

negative effects on freshwater causing eutrophication, and thus its associated extra costs on disposal and waste treatment are highly undesirable.[7]

Recent research has been focusing on developing environmentally friendly and green chemical conversion coating (CCC) based on zirconium. Other elements have been investigated; for instance, H. Vakili et al. studied cerium-based conversion (Ce) treatment with zinc phosphate post-treatment and found improvements on both corrosion resistance of coated steel and adhesion between the steel and epoxy.[8] However, this process is considered rather time-consuming and not yet applicable for industrial application. Recent research focuses on developing CCC processes such as Zr-based systems that are environmentally friendly, cost-effective, industrially scalable, and providing better anticorrosion properties without changing the mechanical properties of the substrate metals.

Zirconium-based (Zr-based) CCC is one of the most promising technologies. The Zr-based conversion coating is created by simple and effective sol−gel process or immersion in hexafluorozirconic-acid-based (H_2ZrF_6-based) conversion solution.[9−11] Research has also shown that incorporation of the additives in the chemical conversion solution can alter the chemical reactions to further improve the properties of the coatings. Examples include the addition of copper (Cu) ions to provide additional cathodic reaction to improve paint coating; Ni ions to improve barrier properties; and organic compounds to improve adhesion and coating density.[5,12−14] In particular, the composition and morphology of Zr-based conversion coating with Cu ion additives are effective for a range of important industrial alloys such as steels and aluminum (Al) alloys.[7,15−17] Research showed that the main components of the coating are ZrO_2 and Cu-rich clusters which are randomly distributed on top of the ZrO_2 layer.[16] J. Cerezo et al.[18] observed, by X-ray photoelectron spectroscopy (XPS), the dissolution of iron (Fe) from the steel during the conversion process and the formation of iron oxide, FeOOH, and FeF_3 under ZrO_2 layer. The majority of the previous research on zirconium-based conversion coatings has focused on the composition and structure or on improvements to the system to increase coating performance parameters. Despite the efforts, the kinetics of the film growth, elemental evolution, coating morphology, and composition with additives, as well as the local structure of the coating remain unclear, which all have great impacts on the properties of the coatings.

In this study, a novel CCC process based on hexafluorozirconic acid (H_2ZrF_6) with Cu additive conversion surface treatment for low carbon steel (LCS) was investigated with an emphasis on understanding kinetics of film growth, and elemental and chemical evolution during coating deposition. The radii and density evolution of Cu-rich clusters on the surface of the samples as a function of treatment time and temperature were quantified to model the cluster growth. As there is an interest in combining different synchrotron X-ray techniques as a multimodal approach to analyze thin film,[19−21] the X-ray fluorescence signal evolution of the chemical elements during coating deposition via *in situ* synchrotron X-ray fluorescence microscopy was analyzed. In addition, chemical composition of coating prepared in different conditions was studied by X-ray absorption near edge structure (XANES) and also complemented by laboratory X-ray photoelectron spectroscopy (XPS). Prior work highlights the effectiveness of using zirconium-based solution for conversion coating process.[2,11,14] Here in the work, a different zirconium-based solution that contains Cu ions was used. Prior work conducted in our laboratory showed that the Cu included in the zirconium oxide conversion coating layer provides improved bonding to the base steel substrate and within the zirconium oxide matrix. The current investigations presented are intended to characterize the copper species present in the zirconium oxide coatings, identify structural features, and study the mechanism of deposition. Furthermore, this work seeks further discussion on the kinetics of film growth through surface morphology of coatings forming in different time and temperature; for the first time, the elemental change in Zr-based conversion coating was observed *in situ* by synchrotron X-ray technique during deposition. The work also highlights the use of X-ray absorption spectroscopy and XPS to characterize both surface and bulk chemical composition of the coating as complementary methods; together a multimodal X-ray analysis approach provides a comprehensive analysis on the film growth and chemical composition. The results revealed the mechanism of the Zr-based coating formation and could guide the design of better-performing Zr-based surface nanocoating CCC processes. The methodology used in study of the complex coating formation and chemical and morphological evolution can also be applied to other CCC processes and surface treatment in general.

2. EXPERIMENT AND CHARACTERIZATION

2.1. Substrate Preparation. LCS sheets, cold rolled steel 1008, were purchased from ACT Test Panels. The surface chemical composition was characterized by laboratory XRF given in Table S1 (Supporting Information). The LCS samples were cut to 5 mm × 5 mm, mechanically polished with SiC papers in subsequent steps, and then polished down to 1 μm surface roughness by diamond paste. The samples were then cleaned in isopropanol (IPA) with ultrasonic bath for 15 min to remove the polishing residue. The polished LCS samples were then dried by compressed air.

2.2. Surface Treatment Solution Preparation. The alkaline cleaner solution, Bonderite C-AK T51 (Henkel Corporation, Madison Heights, MI), contains potassium hydroxide, sodium hydroxide, sodium nitrite, and sodium silicate, producing pH = 11.7. The hexafluorozirconic acid (H_2ZrF_6) with cupric nitrate additive surface conversion coating solution, Bonderite M-NT 1820, was provided by Henkel Corporation (Madison Heights, MI). The Cu in the

DOI: 10.1021/acsanm.8b02309
ACS Appl. Nano Mater. 2019, 2, 1920−1929

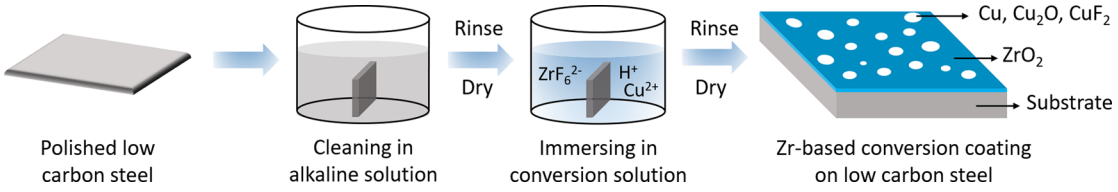

Figure 1. Preparation process of Zr-based conversion coating on LCS.

solution in parts per million (ppm) at level of 10 and the Zr concentration is between 50 and 300 ppm, with a pH = 4.0. The stability of the Zr-based solution is controlled through pH value, free and total fluorine ion concentration, zirconium ion concentration, and temperature. The details of the solution, including compositions, have been published previously.[22]

2.3. Deposition of Conversion Coating. The surfaces of the polished LCS substrates were cleaned by submerging the samples in an alkaline cleaner solution for 120 s at a temperature (T) of 48 °C and rinsing them in DI water for 60 s at T ~24 °C. The samples were then dried by compressed air. The LCS substrates were immersed in hexafluorozirconic acid conversion bath with different conditions according to the treatment parameters listed in Table 1. Samples were treated at 22, 32, and 42 °C, respectively, each temperature for 30, 60, 120, and 240 s. The coating fabrication is shown in Figure 1. One additional condition with 600 s coating at 22 °C was prepared to study the effect of prolonged coating time. During the immersion process, samples were gently agitated in the treatment bath to mimic a typical surface conversion treatment process. Afterward, the treated samples were immersed in deionized (DI) water at T ~24 °C for 60 s and dried under compressed air.

2.4. Surface Morphological Evolution Characterization. Scanning electron microscopy (SEM, JEOL 7600F) was used at 20 keV accelerating voltage to characterize the surface morphology of each sample treated in different conditions. SEM images were taken at three different locations on each sample, with distance between two locations >400 μm. In each of the SEM images, the clusters on the sample surface were statistically analyzed by ImageJ[23] software according to threshold segmentation method to identify the individual clusters on the surface of the samples. The SEM images were cropped to 5 × 5 μm^2 in ImageJ. After segmentation, the cluster size distribution and the number of clusters were quantified, and the results from the three SEM images were averaged. Each image was segmented with a set of maximum and minimum threshold values to determine the variation because of segmentation. The noise was filtered out by determining the minimum size of clusters via examining the images. Each of the particles' size was then determined by pixel counting from the segmented images to quantify the particle size distribution. The particle radii were quantified by assuming each of the particles to be circular in shape, and the radii of an in-plane circumventing circle were then calculated from the area of each particle. The nearest neighbor distance between the center of the particles was quantified using the Nearest Neighbor Distance plug-in[24] as a function of treatment time and temperature. The radii distribution and best power-law fitting of average radii (r) of each sample as a function of time (t) is in the form $r^n \sim t$.

2.5. *In Situ* Synchrotron X-ray Fluorescence Microscopy (XRF). The *in situ* liquid flow cell (modified Hummingbird Scientific cell adopted for synchrotron experiments) comprised two silicon nitride (Si_3N_4) window chips whose thickness were ~30 nm, which allowed gas or liquid flowing between the two chips where the specimen is mounted. The chips were of two different sizes, designated "small" and "large". The Si_3N_4 window allowed the incident X-ray beam and the X-ray fluorescence beam to penetrate into the cell. The window size was of 200 μm × 60 μm (horizontal × vertical). Then two chips were fixed by O rings and a 1 μm tall spacer to define the path for liquid or gas to flow through (Figure 2). In addition, both chips were cleaned by plasma cleaning process immediately prior to mounting the specimen to ensure that their surfaces are hydrophilic and could be wet by the solution.[25] After that, the specimen was welded on the edge of the window at the flat side of the small chip (Figure 2) by a lift-out process described below.

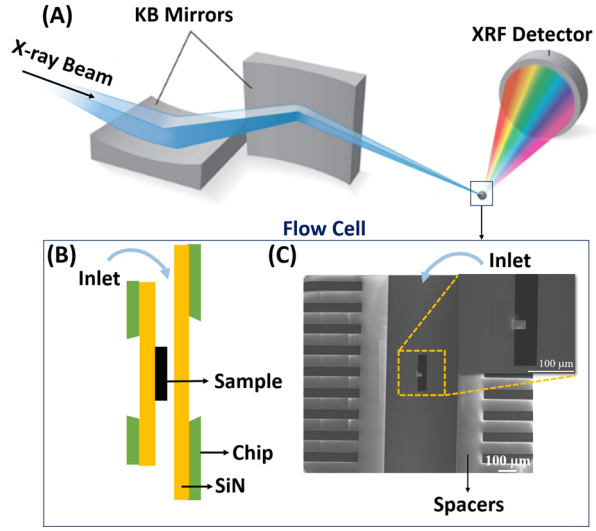

Figure 2. *In situ* experiment set up. (A) Schematics showing the SRX beamline layout. (B, C) Side and front view of the flow cell.

Focused ion beam–scanning electron microscopy (FIB–SEM) lift-out process was used to prepare a LCS specimen (20 × 30 μm^2) at the energy of 30.0 keV. Then we lifted out the specimen with an Omniprobe needle and mounted it on a transmission electron microscopy (TEM) grid. Then the thickness of specimen was finally milled at 5 keV to be <1 μm, to minimize the signal from LCS specimen during the *in situ* experiment. After that, the LCS specimen was removed from TEM grid and attached by using platinum (Pt) weld into a Si_3N_4 window chip for *in situ* cell. The above sample preparation process is shown on Figure 2.

In situ synchrotron X-ray fluorescence (XRF) and micro X-ray absorption near edge structure spectroscopy (μ-XANES) of Zr K-edge were performed by using submicron resolution X-ray spectroscopy (SRX, 5-ID) beamline at National Synchrotron Light Source II (NSLS-II) of BNL.[26] The incident X-ray

DOI: 10.1021/acsanm.8b02309
ACS Appl. Nano Mater. 2019, 2, 1920–1929

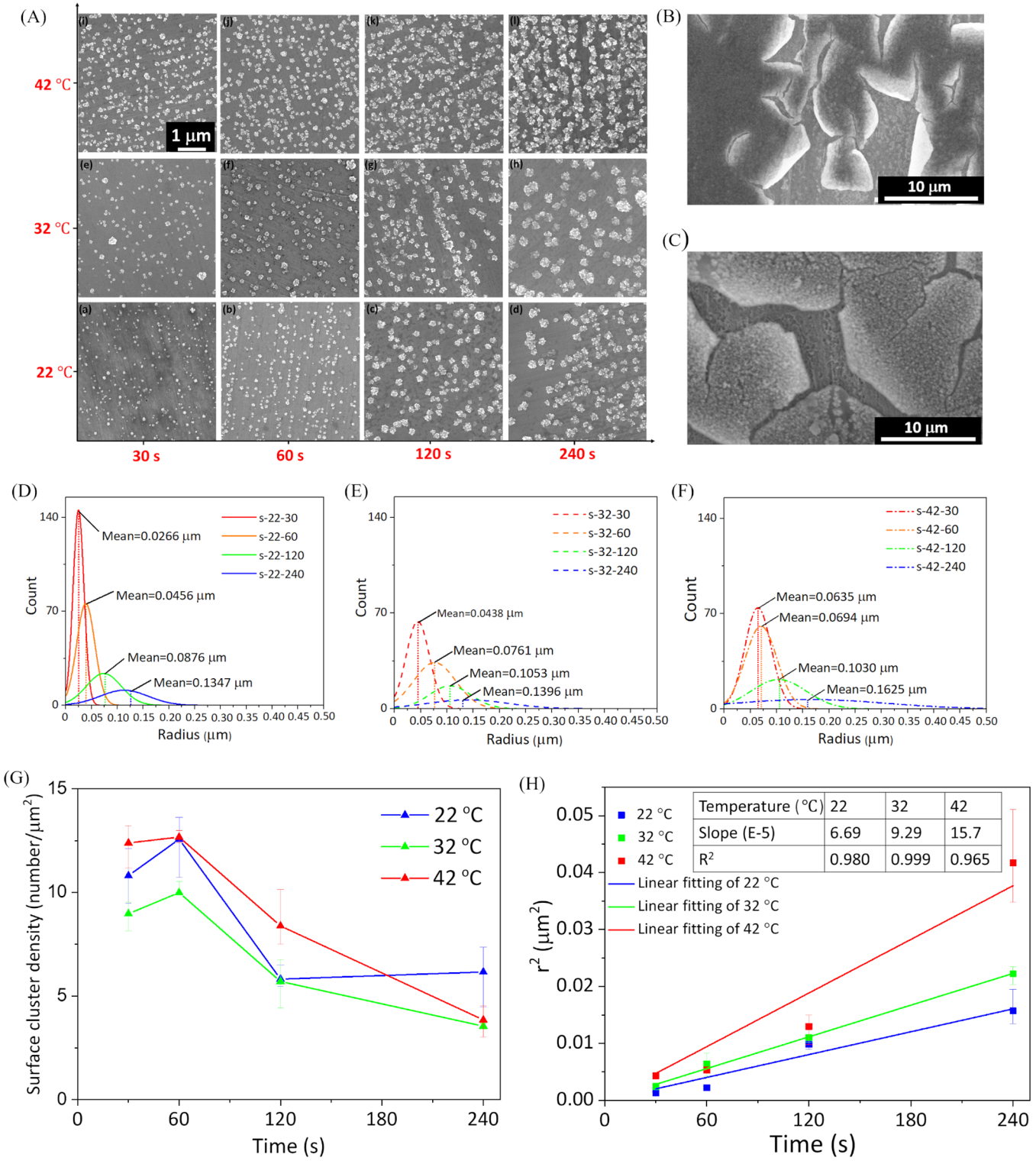

Figure 3. (A) Surface morphology of major samples. (B, C) Morphology of s-22-600, delamination shows on the surface. (D–F) Cluster radii distribution at one location and one segmentation value of major samples. (G) Number of clusters per unit area evolution. (H) Best power (n = 2) of radii against treatment time at different temperature. The lines represent least-squares fit of a linear function of the data points.

energy was set to 19.0 keV for measuring fluorescence signals from Zr, Cu, Fe, and Zn. A set of Kirkpatrick–Baez focusing mirrors were used to focus the X-ray beam down to ~1 × 1 μm^2 at the points of interest of the sample.[27,28]

Before and after the solution treatment experiment, XRF elemental mapping with 1 μm step size was conducted on an area of 50 × 40 μm^2, including the solution and the FIB-milled sample inside the *in situ* cell. PyXRF, an X-ray fluorescence analysis package developed at NSLS-II of BNL,[29] was used to analyze the elemental distribution in the sample before and after treatment. To determine global fitting parameters, the XRF spectrum, summed up over the entire sample, was fitted according to the nonlinear least-squares method to determine global fitting parameters; this includes the background fitting,

DOI: 10.1021/acsanm.8b02309
ACS Appl. Nano Mater. 2019, 2, 1920–1929

and further details can be found in the prior work.[30] The XRF spectrum from pixel fitting was then fitted to quantify the XRF peak area of each element, corresponding to the relative concentration of the element for a given pixel. The XRF elemental distribution maps for Zr, Cu, and Fe were obtained.

The *in situ* conversion coating formation experiment was carried out by injecting the conversion treatment solution (pH = 4.6) utilizing a syringe pump (Chemyx), with tubing connected to the *in situ* flow cell device. The flow rate was set to 3 μL/min. The total volume of conversion treatment solution was about 250 μL. During *in situ* XRF experiment, coarse XRF imaging scans of 32 × 16 (horizontal × vertical) were collected repeated on the same area with a large step size of 8 μm for better time resolution. There was a total treatment time of 2228.1 s, followed by flowing DI water of 1917.8 s to purge the treatment solution to stop the surface treatment process. PyXRF batch fitting was conducted on all the XRF spectra collected during the *in situ* experiment to determine the concentration change of Zr, Cu, Fe, and Zn during coating formation process.

2.6. Grazing Incident Angle X-ray Absorption Near Edge Structure Spectroscopy. To further analyze the chemical composition of the Zr and Cu contents in the coatings, XANES spectroscopy of coated samples (s-32-30 and s-32-240) was conducted at the Beamline for Materials Measurement (BMM) at NSLS-II of BNL. A grazing incident geometry was used at BMM to increase the surface sensitivity of the measurement. To mitigate the Bragg diffraction signals from the substrate, samples were rotated during the X-ray absorption spectroscopy (XAS) data collection;[31] the Bragg diffraction signals became background and can be removed during the postprocessing. XAS spectra of both the Zr and Cu K-edges on each sample were collected by scanning the monochromator. In addition, the XAS spectra of standard samples, including Zr foil, Cu foil, ZrO_2, CuO, and Cu_2O powders, were measured in transmission mode.

Athena software package was used to analyze the XANES data. First, four Zr K-edge scans and 40 Cu K-edge scans of each sample were averaged to improve the signal-to-noise ratio. Background subtraction was performed, and normalization was conducted by subtracting the curvature of the regressed quadratic and the difference between the lines fitted to pre- and postedge regions.[32] The XANES spectra of the samples can then be compared with the spectra from the standard samples for fingerprinting and linear combination fitting.

2.7. X-ray Photoelectron Spectroscopy (XPS) Measurement and Analysis. The XPS experiments were carried out in an ultrahigh vacuum (UHV) system with base pressures <2 Torr equipped with a hemispherical electron energy analyzer (SPECS, PHOIBOS 100) and twin anode X-ray source (SPECS, XR50). Al Kα(1486.6 eV) radiation was used at 10 kV and 30 mA. The angle between the analyzer and X-ray source was 45°, and photoelectrons were collected along the sample surface normal. To determine compositions and their chemical states as a function of depth from the original surface, surface layer was removed by Ar^+ ion sputtering with 1500 V beam voltage. Depth profile XPS was repeated at each depth. Analyses of the Zr 3d XPS and Cu LMM Auger peak were performed utilizing CasaXPS software. The C 2p peak at 284.5 eV was applied to calibrate the energy shift with Shirley background subtraction.

3. RESULTS AND DISCUSSION

3.1. Surface Morphology and Elemental Distribution. The morphological evolution with treatment time and temperature was quantified by analyzing the SEM images. Figure 3A shows representative SEM images of samples from each of the coating conditions. Figure S1 (Supporting Information) confirms that the cluster had higher Cu intensity, and the thickness of the coating on s-32-120 was ∼60 nm. The thickness and roughness of the coating may vary from different conditions. Other work suggested that the surface roughness increases with increasing time.[33] Considering that the roughness may influence the adhesion of the subsequent surface paint, this surface roughness may be of interest of the field to study as future work.

Qualitatively, the clusters were homogeneously distributed on the surface with similar sizes. For the same treatment temperature, the size of the Cu cluster grew as a function of treatment time. With the clusters' growth, neighboring clusters would agglomerate together to form a larger cluster. Similarly, the comparison between samples at same treatment time but with different temperature showed the size of clusters increased with the increased temperature as well. Overall, higher temperature and longer treatment time would lead to the growth of the Cu-rich clusters on the surface. Prior experimental results showed that the surface treatment with Cu ion additives would only enhance the adhesion of the organic paint within a window of treatment time and temperature. The results showed that this correlation may be due to optimizing the surface roughness for the organic paint to bind to the substrate, while avoiding overcoating the surface with high density of the Cu clusters.

To investigate the morphology of the samples treated for longer time, the surface of the sample treated at 22 °C for 600 s is shown in Figure 3B,C. The results show that samples treated with longer time may develop cracks or delamination in the coating. Other studies reported similar surface morphological change caused by dehydration and shrinkage during exposure to the vacuum of the SEM chamber or open dry air.[12,15,34] However, the surface cracks and delamination observed here might not be introduced by the SEM vacuum environment or the electron beam as it was also observed by XRF microscopy of sample s-22-600, shown in Figure S2 (Supporting Information). The cracks and delamination may be due to the thicker film's stress, caused by either the mismatch of lattice constant between the substrate and the film, or the nonuniform thickness across the film which is much more obvious in samples treated for longer time or higher temperature.

The time and temperature dependence of the cluster growth were further quantified. The time evolution of the radii distribution of the cluster, fitted with Gaussian distribution, is shown as Figure 3D−F. The raw data of the radii distribution as a function of treatment time and temperature are shown in Figure S3, including median, mean, and standard deviation (σ) of each fitted Gaussian Curve. Table S2 provides the number of clusters analyzed for each sample. The cluster radii in the samples treated with shorter time were smaller than the ones treated with longer time; however the number of clusters was greater at the initial stage of the treatment as shown in Figure 3G. The results indicate that, at the early stage of the surface treatment, the nucleation rates were high while, at the later treatment stages, the growth and merging rates of the clusters

DOI: 10.1021/acsanm.8b02309
ACS Appl. Nano Mater. 2019, 2, 1920−1929

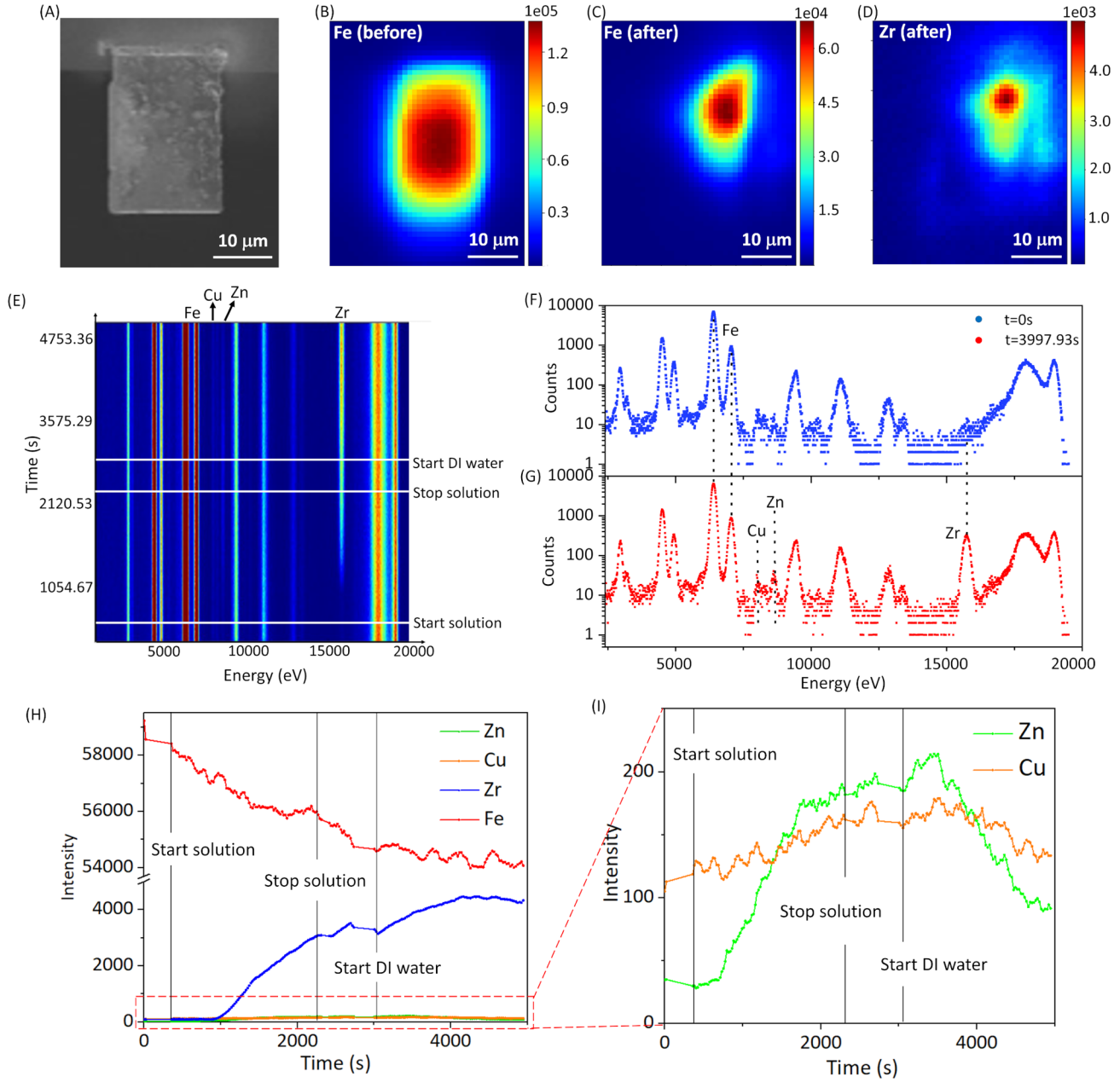

Figure 4. (A) SEM image of sample. (B) Fe XRF mapping before experiment. (C, D) Fe and Zr XRF mapping after the experiment. (E) Fluorescence intensity of different elements during treatment process. (F, G) X-ray fluorescence spectrum at t = 0 and t = 3997.9 s, Fe, Cu, Zn and Zr K-edge peak are marked with dotted lines. (H, I) X-ray fluorescence intensity change of Zr, Cu, Fe, and Zn.

were faster than the rates of nucleation. As the treatment time increases, both nucleation of new clusters and growth of the existing clusters occurred. The nearest neighbor distances between the center of particles for different treatment conditions are shown in Figure S4. The increase of the distance between particles is consistent with the merging of the clusters. Hence, samples treated with longer time have a broad distribution of the cluster sizes, and the average size of clusters increases with the treatment time. The difference of cluster distribution at different locations within the samples and from different segmentation values is negligible as shown in Figure S5 with sample s-32-30 as an example.

The power law of the radii (r) was determined by fitting the r^n vs treatment time (t) with different n values, from n = 1−4, corresponding to different mechanisms. The fitting was constrained to intercept at the origin, which corresponds to that at t = 0, r = 0. Best linearity corresponding to the growth exponents for three temperatures are n = 2, but the slope increases with temperature as shown in Figure 3H. In two dimensions, reaction-limited growth typically follows a power law of $r^2 \sim t$, and a power law with n = 3 typically suggests diffusion-controlled growth.[35,36] The growth mechanism is correlated to reaction-controlled growth. Different power-law (n = 1-4) fittings are shown in Figure S6.

3.2. *In Situ* Concentration Evolution and Morphology Change. XRF mapping of Fe on sample prior to the surface treatment corresponds directly to the size of the sample as shown in Figure 4A,B. After the surface treatment, Figure 4C,D shows the XRF mapping of both Fe and Zr morphology. The morphology evolution from Fe XRF mapping shows that Fe

DOI: 10.1021/acsanm.8b02309
ACS Appl. Nano Mater. 2019, 2, 1920−1929

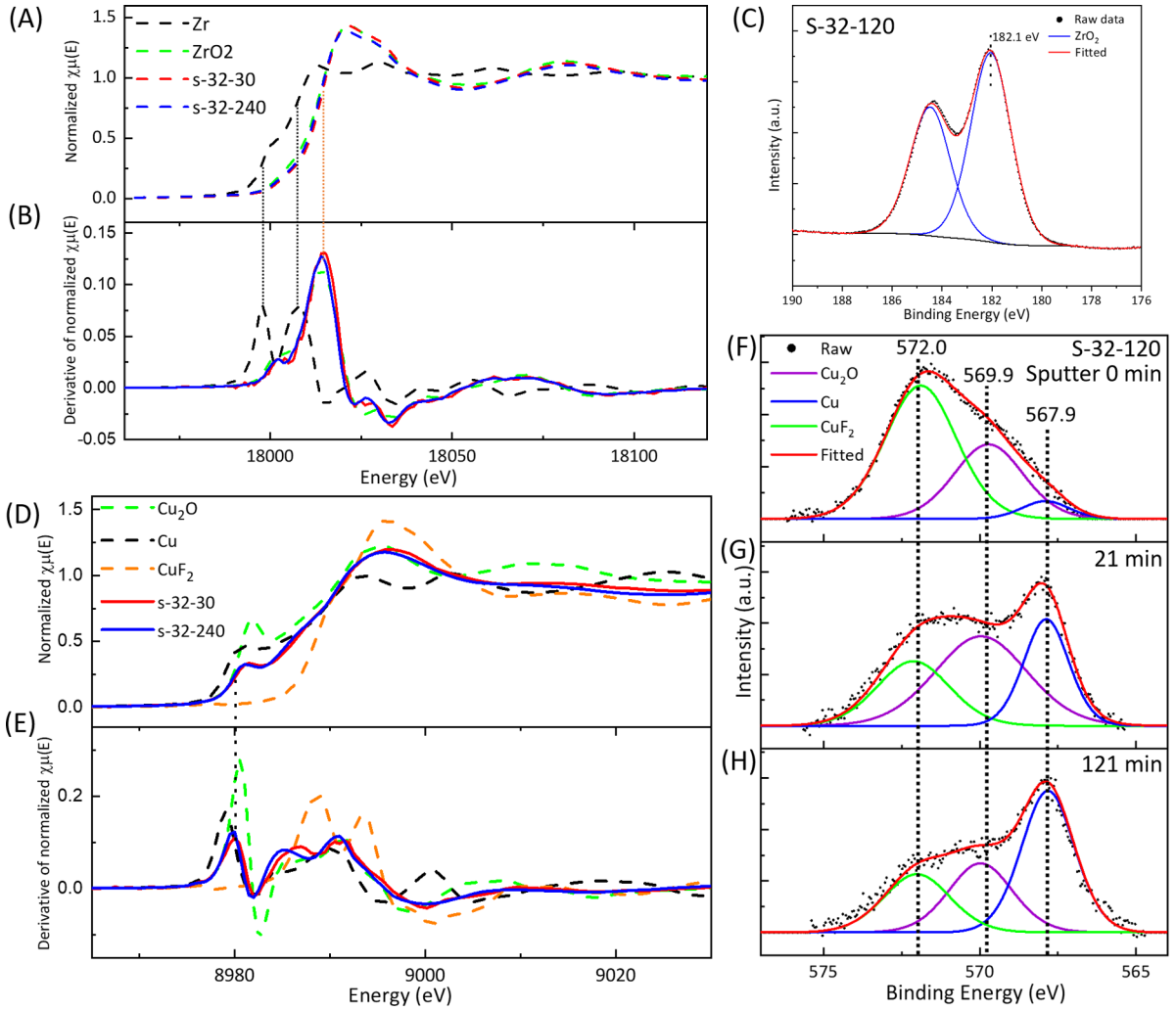

Figure 5. (A, B) Normalized XANES and first derivative XANES spectra of s-32-30, s-32-240, Zr foil, and ZrO_2 standards. (C) Zr 3d XPS of s-32-120. (D, E) Normalized XANES and first derivative XANES spectra of s-32-30, s-32-240, Cu, Cu_2O, and CuF_2 standards. (F–H) Depth-profiling Cu LMM Auger XPS of s-32-120 with different sputtering time.

has been etched during the surface treatment process indicating competing mechanisms between surface coating and etching of the substrate; as a result, the remaining Fe substrate showed a thicker central region with higher XRF intensity, whereas the edges have been etched further, with lower XRF intensity. Meanwhile, the Zr morphology distribution is colocalized with the distribution of Fe, indicating that the Zr conversion coating was formed on the steel substrate.

Figure 4E shows the evolution of XRF spectra as a function of treatment time which shows the elemental composition in the solution and on the sample changed during the *in situ* experiment. Figure 4F,G shows the XRF spectra of the sample before (t = 0 s) and after (t = 3997.9 s) the surface treatment. The XRF spectrum from the post-treatment (Figure 4G) clearly shows the new peak of Zr K-edge, which was not present prior to the surface treatment (Figure 4F).

The evolution of the elemental concentration during the surface treatment was then quantified as the function of the treatment time. We first differentiated three different regions in the XRF mapping: sample, solution, and interface area by using the Fe XRF mapping of the first *in situ* scan as shown in Figure S7, because the Fe signal could only be detected on the sample. The XRF signal intensity of each element of every scan was then fitted in PyXRF with the batch fitting mode in Python environment and plotted as a function of time as shown in Figure 4H,I.

The Zr XRF signal did not increase immediately as the starting point of the solution injection. One possible reason is that it takes time for the solution to flow from the syringe pump into the *in situ* cell. In addition, when the solution first contacts the surface of the substrate, oxygen reduction ($O_2 + 2H_2O + 4e^- \rightarrow 4OH^-$) and hydrogen evolution ($2H^+ + 2e^- \rightarrow H_2$) would take place at microcathodic sites which could lead to local pH increase.[37] Li et al. found that the interfacial pH shifted from 3.9 to about 7 during the first 2 min of hexafluorozirconic acid treatment by *in situ* pH measurement monitoring conversion coating formation on aluminum alloy by using tungsten microelectrode.[38] Then, the hydrolysis reaction takes place in the solution containing ZrF_6^{2-} ($ZrF_6^{2-} + 4OH^- \rightarrow ZrO_2{\cdot}2H_2O + 6F^-$) driven by the increase of pH, which also balances cathodic reactions to a certain degree and forms a hydrated zirconia film. The reason why the intensity of Zr keeps increasing even after starting injecting DI water is because DI water from the syringe pushes remaining H_2ZrF_6 solution in the tube into the *in situ* cell to interact with the

DOI: 10.1021/acsanm.8b02309
ACS Appl. Nano Mater. 2019, 2, 1920–1929

sample first. Toward the end of the reaction the Zr signal starts to drop, indicating that some of the Zr XRF signal increase was from the solution and not entirely from the formation of the surface coating that contains Zr.

The Cu XRF intensity also increased during the surface treatment process, and the timing qualitatively correlates with the growth of the Zr XRF signal. The Cu XRF signal is noisy, because the amount of Cu ions in the solution is low. The chemical constitutes of the Zr and Cu will be discussed by utilizing XANES later in section 3.3.

The intensity of Fe decreases which means Fe is partially dissolved during *in situ* process, because anodic reaction of Fe ($Fe \rightarrow Fe^{2+} + 2e^-$) could help the precipitation of Zr hydroxide to form the Zr-based coating layer at the initial stage of the conversion coating. The transmission of Fe K-α through ZrO_2 (thickness ~100 nm) is ~99%, which means that ZrO_2 does not block X-ray fluorescence signal of Fe. One additional element that was in the solution was Zn ion, which can improve coating properties such as corrosion resistance.[22] From Figure 4I, when solution flew through the surface of the steel, the concentration of Zn increased; however when the *in situ* cell was purged with DI water, the concentration of Zn decreased. In addition, no Zn XRF signal was detected from the fine XRF mapping post-treatment. These results indicate that the Zn ions, while present in the solution, did not codeposit with the Zr and Cu ions, during the surface conversion process.

3.3. XANES and XPS of Zr and Cu in Surface Coating.

3.3.1. Zr-Compound Film. XANES spectra comparisons between unknown samples and well-characterized standard compounds are often conducted to fingerprint the chemical compositions and oxidation states of the unknown samples. Zr K-edge (17998 eV) XANES spectra of Zr foil, ZrO_2 powder standard, and sample s-32-30 and s-32-240 were measured to characterize influence of treatment time. The normalized XANES spectra and their first derivatives are shown in Figure 5A,B. The edge energy position shift between the samples and Zr foil reference indicates that the valence state of Zr in the samples is not Zr(0). Meanwhile, the prominent postedge peak of the samples and ZrO_2 standard are the same (18019.5 eV), with nearly identical spectra shapes. This suggests that the valence state is Zr(IV), and the chemical component in the coating is ZrO_2. The XPS Zr 3d core level spectrum is also shown in Figure 5C, with a fitting of doublets. The binding energy of Zr $3d_{5/2}$ electron was determined to be 182.1 eV, consistent with ZrO_2.[39] Furthermore, from Figure S8, samples prepared at 32 °C for different surface treatment times from 30 to 60, 120, and to 240 s shared the same edge position with ZrO_2 standard and similar XANES spectra shapes.

3.3.2. Cu-Compound Surface Clusters. The Cu oxidation states and chemical constitutes are also of interest. Khun et al. applied XPS to investigate steels with similar Zr conversion coating for different treatment time and found that CuO and Cu_2O were incorporated in the coating.[33] According to their work, Cu^{2+} in the solution first has a cathodic reaction ($Cu^{2+} + 2e^- \rightarrow Cu$) and becomes a metallic form. Immediately, Cu is oxidized and forms CuO and Cu_2O. Here we utilized Cu XANES and XPS depth profile to investigate the chemical compositions of the Cu-rich clusters in the film.

Figure 5D,E shows Cu K-edge (8979 eV) XANES spectra and first derivatives of sample s-32-30, s-32-240, Cu, Cu_2O, CuO, and CuF_2 standards. Both the pre-edge positions and the prominent postedge peaks of the samples are similar to Cu_2O and Cu foil, indicating the presence of Cu_2O and metallic Cu. The first peak in the derivative of Cu_2O XANES spectra as shown in Figure 5E is at 8983 eV, corresponding to an electronic transition from 1s to 4p concurrent with ligand to metal charge transfer character,[40,41] while the first peaks of samples slightly shift to lower energy. However, from XANES data, we cannot determine the presence of CuO and CuF_2; XPS was thus used to study the composition of the Cu compounds.

The depth-profiling XPS was used to further analyze the Cu compounds evolution along with the depth of the film (Figure 5F−H. Cu LMM Auger spectra were fitted well using three individual peaks at 569.9±0.1 eV (Cu_2O), 572.0±0.1 eV (CuF_2), and 567.9±0.1 eV (Cu).[42,43] Surface Cu 2p core level XPS spectra were fitted with CuF_2 peak as one compound (Figure S9). Hence, for Cu-rich clusters, metallic Cu forms in core area because of cathodic reaction of Cu ions. When contacting with the air, Cu was oxidized into Cu_2O in outer shell. In addition, the CuF_2 distributed in the cluster because F ions are in the surface treatment solution to control the pH value. While reports showed that releasing high concentration of fluoride will negatively influence environment, it is worth noting that fluoride is being used in many consumer applications, including its use in U.S. water supply to improve dental health and toothpaste. Overall, the fluoride influence on environment is very limited from zirconium conversion coating. First, the concentration of fluoride is very low in the solution compared to conventional zinc phosphate solution (F > 100 ppm), not to mention the significant amount of phosphate in zinc phosphate solution which can contribute to eutrophication. The development of the zirconium-based conversion coating solution does not contain phosphate ion and has a much lower concentration of fluoride; as such, it is viewed as a safer alternative to zinc-phosphate-based conversion coating solutions. Furthermore, in industry, the zirconium conversion solution is treated at the application facilities water treatment system to ensure proper disposal. The concerns regarding potential exposure for the workers using the solution are also mitigated by wearing appropriate personal protective equipment. To further analyze the ratio of three Cu compounds, a linear combination fitting (LCF) of XANES was conducted (Figure S10). s-32-30 contains Cu (29%), Cu_2O (36%), and CuF_2 (36%), and s-32-240 has Cu (35%), Cu_2O (31%), and CuF_2 (34%).

4. CONCLUSION

We investigated the morphology and chemical state evolution of zirconium conversion coating forming in different time and temperature on LCS characterizing by SEM, XRF mapping, and XAS. The coating formation kinetics could be modeled as the reaction-controlled mechanism. Surface morphology showed that the average cluster radii increased with time and temperature; however, cluster density increased at the initial stage but decreased with longer treatment time because the clusters grew larger and merged together. Moreover, XRF intensity change of Zr, Cu, Fe, and Zn during *in situ* coating deposition process showed that Zr and Cu gradually formed on LCS; however, to help the precipitation of the film, Fe dissolved in the solution. Particularly, elemental mapping showed that Zr is highly correlated to Fe meaning coating was uniformly forming on the substrate. From XANES comparison between samples and reference materials, we could conclude H_2ZrF_6 in the solution has formed ZrO_2 layer on the steel at

DOI: 10.1021/acsanm.8b02309
ACS Appl. Nano Mater. 2019, 2, 1920−1929

32 °C in different time. For Cu ions in the solution, it mainly took cathodic reaction to form metallic Cu inner following oxidizing to form Cu_2O at outermost shell. As the XPS depth-profiling showed different compositions from the surface to the interior of the film, further analysis concerning the effect of treatment time and temperature on the elemental distribution could be carried out. Therefore, from this work, the Cu cluster on the Zr-based conversion coating formation was reaction-controlled mechanism. Chemical reactions occurred during coating deposition were observed; the final composition formed steel was characterized to be ZrO_2 in the film and Cu_2O, Cu, and CuF_2 in the clusters. Future work on quantifying the coating thickness and roughness shall be conducted as a function of conversion treatment time and temperature to further understand the film growth mechanism, functionalities, and potential degradation mechanism. A precipitation of compounds is time and temperature dependent; future work may further analyze the composition of the films and clusters if longer treatment or higher treatment temperature is required as well. Similar consideration shall also be applied when developing new conversion coating solutions.

■ ASSOCIATED CONTENT

Supporting Information

The Supporting Information is available free of charge on the ACS Publications website at DOI: 10.1021/acsanm.8b02309.

Further details on experiments and analysis can be found in the Supporting Information, including elemental composition, surface and cross-section morphology, XRF mappings, raw data of cluster radii distribution, numbers of clusters, nearest neighbor distance, segmentation and location influence, power-law fitting (n = 1-4), XANES of samples treated in 32 °C, Cu 2p XPS spectra, and linear combination fitting result (PDF)

■ AUTHOR INFORMATION

Corresponding Author

*E-mail: karen.chen-wiegart@stonybrook.edu.

ORCID

Xiaoyang Liu: 0000-0002-9326-2135

Funding

X.L. and K.C.-W. acknowledge the support by the Department of Materials Science and Chemical Engineering, the College of Engineering and Applied Sciences and Stony Brook University. The work is in part supported by Henkel Corp., Award 81113. This research used resources, Submicron Resolution X-ray Spectroscope (SRX, 5-ID) and Beamline for Materials Measurement (BMM, 6-BM) of the National Synchrotron Light Source II, a U.S. Department of Energy (DOE) office of Science Users Facility operated for the DOE office of Science by Brookhaven National Laboratory under Contract DE-SC0012704. This research used resources of the Center for Functional Nanomaterials, which is a U.S. DOE Office of Science Facility, at Brookhaven National Laboratory under Contract DE-SC0012704.

Notes

The authors declare no competing financial interest.

■ ACKNOWLEDGMENTS

The authors thank Gwen Wright, Fernando Camino (Center for Functional Nanomaterials, CFN), and Chonghang Zhao for assisting SEM, EDS, and FIB−SEM. Li Li (National Synchrotron Light Source II, NSLS-II) is acknowledged for developing XRF analysis software, PyXRF. The development of PyXRF is supported by LDRD grant, funded by Brookhaven National Laboratory. The authors thank Yong Chu for providing the *in situ* cell used for the experiment. The authors appreciate the support from Juergen Thieme, Garth Williams, and Andrew Kiss for SRX beamtime, and mechanical support from Michael Maklary (NSLS-II). We thank Prof. Gary Halada and Michael Cuiffo for the access to the laboratory XRF system as well as the assistance on the measurements.

■ REFERENCES

(1) Prasai, D.; Tuberquia, J. C.; Harl, R. R.; Jennings, G. K.; Bolotin, K. I. Graphene: Corrosion-Inhibiting Coating. *ACS Nano* **2012**, *6*, 1102−1108.

(2) Asemani, H. R.; Ahmadi, P.; Sarabi, A. A.; Mohammadloo, H. E. Effect of zirconium conversion coating: Adhesion and anti-corrosion properties of epoxy organic coating containing zinc aluminum polyphosphate (ZAPP) pigment on carbon mild steel. *Prog. Org. Coat.* **2016**, *94*, 18−27.

(3) Ehsani, A.; Mahjani, M. G.; Hosseini, M.; Safari, R.; Moshrefi, R.; Shiri, H. M. Evaluation of Thymus vulgaris plant extract as an eco-friendly corrosion inhibitor for stainless steel 304 in acidic solution by means of electrochemical impedance spectroscopy, electrochemical noise analysis and density functional theory. *J. Colloid Interface Sci.* **2017**, *490*, 444−451.

(4) Hao, T. H.; Liu, X. Y.; Hu, G. H.; Jiang, T.; Zhang, Q. C. Preparation and characterization of polyurethane/POSS hybrid aqueous dispersions from mono-amino substituted POSS. *Polym. Bull.* **2017**, *74*, 517−529.

(5) Milosev, I.; Frankel, G. S. Review—Conversion Coatings Based on Zirconium and/or Titanium. *J. Electrochem. Soc.* **2018**, *165*, 127−144.

(6) De, S.; Lutkenhaus, J. L. Corrosion behaviour of eco-friendly airbrushed reduced graphene oxide-poly(vinyl alcohol) coatings. *Green Chem.* **2018**, *20*, 506−514.

(7) Adhikari, S.; Unocic, K. A.; Zhai, Y.; Frankel, G. S.; Zimmerman, J.; Fristad, W. Hexafluorozirconic acid based surface pretreatments: Characterization and performance assessment. *Electrochim. Acta* **2011**, *56*, 1912−1924.

(8) Vakili, H.; Ramezanzadeh, B.; Amini, R. The corrosion performance and adhesion properties of the epoxy coating applied on the steel substrates treated by cerium-based conversion coatings. *Corros. Sci.* **2015**, *94*, 466−475.

(9) Fedrizzi, L.; Rodriguez, F. J.; Rossi, S.; Deflorian, F.; Di Maggio, R. The use of electrochemical techniques to study the corrosion behaviour of organic coatings on steel pretreated with sol-gel zirconia films. *Electrochim. Acta* **2001**, *46*, 3715−3724.

(10) Gusmano, G.; Montesperelli, G.; Rapone, M.; Padeletti, G.; Cusma, A.; Kaciulis, S.; Mezzi, A.; Di Maggio, R. Zirconia primers for corrosion resistant coatings. *Surf. Coat. Technol.* **2007**, *201*, 5822−5828.

(11) Tepe, B.; Gunay, B. Evaluation of Environmentally Friendly Zr Based Nano Structured Conversion Coating for HRS (Hot Rolled Steel) in Powder Coating. *Defect Diffus. Forum* **2009**, *283−286*, 316−322.

(12) George, F. O.; Skeldon, P.; Thompson, G. E. Formation of zirconium-based conversion coatings on aluminium and Al-Cu alloys. *Corros. Sci.* **2012**, *65*, 231−237.

(13) Chidambaram, D.; Clayton, C. R.; Halada, G. P. The role of hexafluorozirconate in the formation of chromate conversion coatings on aluminum alloys. *Electrochim. Acta* **2006**, *51*, 2862−2871.

(14) Asemani, H. R.; Sarabi, A. A.; Mohammadloo, H. E.; Sarayloo, M. Electrochemical and morphological properties of zirconium conversion coating in the presence of nickel ions on galvanized steel. *J. Coat. Technol. Res.* **2016**, *13*, 883−894.

DOI: 10.1021/acsanm.8b02309
ACS Appl. Nano Mater. 2019, 2, 1920−1929

(15) Lostak, T.; Krebs, S.; Maljusch, A.; Gothe, T.; Giza, M.; Kimpel, M.; Flock, J.; Schulz, S. Formation and characterization of Fe3+-/Cu2+-modified zirconium oxide conversion layers on zinc alloy coated steel sheets. *Electrochim. Acta* **2013**, *112*, 14−23.
(16) Sarfraz, A.; Posner, R.; Lange, M. M.; Lill, K.; Erbe, A. Role of Intermetallics and Copper in the Deposition of ZrO2 Conversion Coatings on AA6014. *J. Electrochem. Soc.* **2014**, *161*, C509−C516.
(17) Cerezo, J.; Vandendael, I.; Posner, R.; de Wit, J. H. W.; Mol, J. M. C.; Terryn, H. The effect of surface pre-conditioning treatments on the local composition of Zr-based conversion coatings formed on aluminium alloys. *Appl. Surf. Sci.* **2016**, *366*, 339−347.
(18) Cerezo, J.; Vandendael, I.; Posner, R.; Lill, K.; de Wit, J. H. W.; Mol, J. M. C.; Terryn, H. Initiation and growth of modified Zr-based conversion coatings on multi-metal surfaces. *Surf. Coat. Technol.* **2013**, *236*, 284−289.
(19) Zhao, C. H.; Wada, T.; De Andrade, V.; Gursoy, D.; Kato, H.; Chen-Wiegart, Y. C. K. Imaging of 3D morphological evolution of nanoporous silicon anode in lithium ion battery by X-ray nano-tomography. *Nano Energy* **2018**, *52*, 381−390.
(20) Woicik, J. C.; Shirley, E. L.; Gilmore, K.; Andersen, K. E.; Hellberg, C. S. Local structural distortions in strained Ba0.5Sr0.5TiO3 thin films. *Phys. Rev. B: Condens. Matter Mater. Phys.* **2017**, *96*, 104111.
(21) Pensel, A.; Peulon, S. In situ XANES measurements during electrodeposition of thin film: Example of birnessite, a promising material for environmental applications. *Electrochim. Acta* **2018**, *281*, 738−745.
(22) Vonk, D., Kapic, E., Goodreau, B., Bobadilla, A. Metal Pretreatment Composition Containing Zirconiusm, Copper, Zinc and Nitrate and Related Coatings on Metal Substrates. U.S. Patent US20120301739A1, 2018.
(23) Rueden, C. T.; Schindelin, J.; Hiner, M. C.; DeZonia, B. E.; Walter, A. E.; Arena, E. T.; Eliceiri, K. W. ImageJ2: ImageJ for the next generation of scientific image data. *BMC Bioinf.* **2017**, *18*, 529.
(24) Haeri, M.; Haeri, M. ImageJ pligin for Analysis of Porous Scaffolds used in Tissue Engineering. *Journal of Open Research Software* **2015**, *3* (1), e1.
(25) Jiang, H. *Evolution of Surface Morphology and Chemistry in ZnO Thin Films and Steel Surfaces studied by Synchrotron X-ray Spectroscopy and Imaging*. Thesis, MS Stony Brook University, 2016.
(26) Jiang, H.; Chou, K. W.; Petrash, S.; Williams, G.; Thieme, J.; Nykypanchuk, D.; Li, L.; Muto, A.; Chen-Wiegart, Y. C. K. Environmentally induced chemical and morphological heterogeneity of zinc oxide thin films. *Appl. Phys. Lett.* **2016**, *109*, 091909.
(27) Zhao, C. H.; Wada, T.; De Andrade, V.; Williams, G. J.; Gelb, J.; Li, L.; Thieme, J.; Kato, H.; Chen-Wiegart, Y. C. K. Three-Dimensional Morphological and Chemical Evolution of Nanoporous Stainless Steel by Liquid Metal Dealloying. *ACS Appl. Mater. Interfaces* **2017**, *9*, 34172−34184.
(28) Chen-Wiegart, Y. C. K.; Williams, G.; Zhao, C. H.; Jiang, H.; Li, L.; Demkowicz, M.; Seita, M.; Short, M.; Ferry, S.; Wada, T.; Kato, H.; Chou, K. W.; Petrash, S.; Catalano, J.; Yao, Y.; Murphy, A.; Zumbulyadis, N.; Centeno, S. A.; Dybowski, C.; Thieme, J. In *Early Science Commissioning Results of the Sub-micron Resolution X-ray Spectroscopy Beamline (SRX) in the Field of Materials Science and Engineering*, 23rd International Congress on X-Ray Optics and Microanalysis (ICXOM), Brookhaven Natl Lab, NY, Sept 14−18; Brookhaven Natl Lab: New York, 2015.
(29) Li, L. *PyXRF*; GitHub, 2015.
(30) Marquardt, D. W. AN ALGORITHM FOR LEAST-SQUARES ESTIMATION OF NONLINEAR PARAMETERS. *J. Soc. Ind. Appl. Math.* **1963**, *11*, 431−441.
(31) Woicik, J. C.; Gupta, J. A.; Watkins, S. P.; Crozier, E. D. Bond-length strain in buried Ga1-xInxAs thin alloy films grown coherently on InP(001) (vol 73, pg 1269, 1998). *Appl. Phys. Lett.* **1998**, *73*, 2219−2219.
(32) Ravel, B.; Newville, M. ATHENA, ARTEMIS, HEPHAESTUS: data analysis for X-ray absorption spectroscopy using IFEFFIT. *J. Synchrotron Radiat.* **2005**, *12*, 537−541.
(33) Khun, N. W.; Frankel, G. S. Composition and corrosion protection of hexafluorozirconic acid treatment on steel. *Mater. Corros.* **2015**, *66*, 1215−1222.
(34) Zhu, W.; Li, W. F.; Mu, S. L.; Yang, Y. Y.; Zuo, X. The adhesion performance of epoxy coating on AA6063 treated in Ti/Zr/V based solution. *Appl. Surf. Sci.* **2016**, *384*, 333−340.
(35) Lifshitz, I. M.; Slyozov, V. V. The kinetics of precipitation from supersaturated solid solutions. *J. Phys. Chem. Solids* **1961**, *19*, 35.
(36) Wagner, C. Z. *Elektrochem* **1961**, *65*, 581.
(37) Eivaz Mohammadloo, H.; Sarabi, A. A.; Hosseini, R. M.; Sarayloo, M.; Sameie, H.; Salimi, R. A comprehensive study of the green hexafluorozirconic acid-based conversion coating. *Prog. Org. Coat.* **2014**, *77*, 322−330.
(38) Li, L. L.; Desouza, A. L.; Swain, G. M. In situ pH measurement during the formation of conversion coatings on an aluminum alloy (AA2024). *Analyst* **2013**, *138*, 4398−4402.
(39) Dou, X. M.; Mohan, D.; Pittman, C. U.; Yang, S. Remediating fluoride from water using hydrous zirconium oxide. *Chem. Eng. J.* **2012**, *198*, 236−245.
(40) Ravel, B.; Carr, G. L.; Hauzenberger, C. A.; Klysubun, W. X-ray and optical spectroscopic study of the coloration of red glass used in 19th century decorative mosaics at the Temple of the Emerald Buddha. *J. Cult. Herit* **2015**, *16*, 315−321.
(41) Liu, X.; Cui, S. S.; Sun, Z. J.; Ren, Y.; Zhang, X. Y.; Du, P. W. Self-Supported Copper Oxide Electrocatalyst for Water Oxidation at Low Overpotential and Confirmation of Its Robustness by Cu K-Edge X-ray Absorption Spectroscopy. *J. Phys. Chem. C* **2016**, *120*, 831−840.
(42) Platzman, I.; Brener, R.; Haick, H.; Tannenbaum, R. Oxidation of polycrystalline copper thin films at ambient conditions. *J. Phys. Chem. C* **2008**, *112*, 1101−1108.
(43) Sarfraz, S.; Garcia-Esparza, A. T.; Jedidi, A.; Cavallo, L.; Takanabe, K. Cu-Sn Bimetallic Catalyst for Selective Aqueous Electroreduction of CO2 to CO. *ACS Catal.* **2016**, *6*, 2842−2851.

DOI: 10.1021/acsanm.8b02309
ACS Appl. Nano Mater. 2019, 2, 1920−1929